

# Towards a zero magnetic field environment for ultracold atoms experiments

C. Rogora<sup>1</sup>, R. Cominotti<sup>1</sup>, C. Baroni<sup>1</sup>, D. Andreoni<sup>1</sup>, G. Lamporesi<sup>1,2,\*</sup>, A. Zenesini<sup>1,2</sup>, and G. Ferrari<sup>1,2</sup>

<sup>1</sup>*Pitaevskii BEC Center, CNR-INO and Dipartimento di Fisica, Università di Trento, 38123 Trento, Italy and*

<sup>2</sup>*Trento Institute for Fundamental Physics and Applications, INFN, 38123 Trento, Italy*

(Dated: May 1, 2024)

The minimization of the magnetic field plays a crucial role in ultracold gas research. For instance, the contact interaction dominates all the other energy scales in the zero magnetic field limit, giving rise to novel quantum phases of matter. However, lowering magnetic fields well below the mG level is often challenging in ultracold gas experiments. In this article, we apply Landau-Zener spectroscopy to characterize and reduce the magnetic field on an ultracold gas of sodium atoms to a few tens of  $\mu\text{G}$ . The lowest magnetic field achieved here opens to observing novel phases of matter with ultracold spinor Bose gases.

## I. INTRODUCTION

Controlling magnetic fields is critical in many contexts involving fundamental and applied physics experiments and quantum technologies. Often, the performance of a measurement critically depends on the stability against fluctuations of the background magnetic field, as it happens in electron microscopy experiments [1–3], atom interferometry [4], nuclear magnetic resonance [5], atomic clock experiments [6], and ultracold gases experiments involving coherently-coupled BEC mixtures [7–9]. In other contexts, such as zero-field nuclear magnetic resonance [10, 11], the constraint relates to the magnitude of the magnetic field, which generally should be minimized and, depending on the type of measurement, needs to be kept below the threshold values. Historically, the measurement of relatively small magnetic fields is achieved using SQUIDs in a cryogenic environment [12], exploiting atomic coherence in room temperature gas cells [13–15], or atomic spin-alignment [16], with applications in diverse fields, including biomedical imaging [17, 18], metal detection [19, 20], and material characterization [21]. Nowadays, a wide variety of experimental platforms and techniques are available, as described, for instance, in Ref. [22]. In the context of magnetometry, cold gases have been consistently employed as magnetic field sensors [23, 24], in various cases with micrometric scale spatial resolution [25–28].

Finding a way to reduce the magnetic field, control it with high accuracy, and be able to measure such small values would pave the way for the investigation of new physical phenomena, such as the zero-magnetic-field physics of spinor condensates, *i.e.* condensates with a vector order parameter. Spinor condensates can develop different configurations, and their ground state depends on the strength of the interactions between the internal states and on the strength of the externally applied magnetic field, which removes the degeneracy between different spin states [29, 30]. The magnetic field is typically large enough that the corresponding magnetic

energy splitting between spin states dominates over the spin-dependent interaction energy. A regime where the two energies are comparable has been studied with dipolar chromium gases in the presence of magnetic fields of a few tenths of a mG, thanks to the large magnetic moment of chromium atoms [31].

For alkali atoms, the spin-dependent interaction is essentially dominated by the contact interaction, given the negligible contribution of the long-range magnetic dipole coupling [32].

This further reduces the threshold magnetic field below which interesting and unobserved spinor phases are expected [29, 30, 33]. The strength of the magnetic field below which these novel phases appear is known, in the case of the zero spatial mode approximation [33], to be on the order of a few hundreds of  $\mu\text{G}$ . However, this threshold is expected at even lower magnetic fields in the case of spatially extended condensates. Here, the experimental challenge relies on the difficulty of controlling the magnetic field stability at the  $\mu\text{G}$  level and reaching and maintaining such small magnetic field values over the whole extension of the atomic sample both during a single experimental sequence and within different runs.

This work presents an experimental technique for minimizing the magnetic field at the  $10\text{-}\mu\text{G}$  level. Since it is impossible to integrate an external device in the vacuum chamber of ultracold atom experiments to characterize and minimize the field, developing an independent technique for the magnetic field characterization using the trapped atoms as sensors becomes necessary. In particular, we describe an application of Landau-Zener (LZ) spectroscopy [34] over an atomic gas of sodium. Reaching such a low field is possible thanks to the presence of a magnetic shield [35], which demonstrated its efficiency in stabilizing the field in several previous works [8, 9, 36, 37]. The results presented in the following open the way to studying the zero-magnetic-field ground state of an  $F=1$  system.

In Sec. II, we describe the experimental platform. Section III contains the theoretical framework and experimental protocols. In Sec. IV we discuss the results, while in Sec. V we report concluding remarks and outlooks.

---

\* [giacomo.lamporesi@ino.cnr.it](mailto:giacomo.lamporesi@ino.cnr.it)

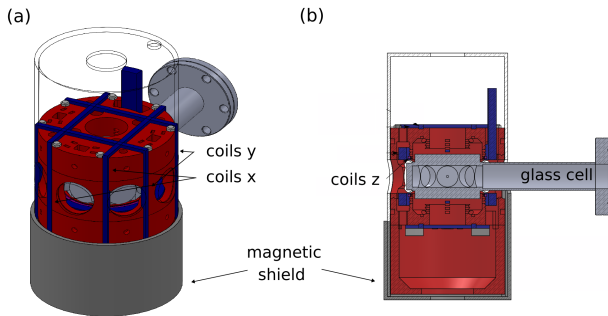


FIG. 1. Schematics of the core setup. (a) The innermost layer of the magnetic shield (dark gray and transparent) contains a 3D-printed plastic support structure for the coils (red), the coils themselves (blue), and the glass cell (light gray). (b)  $yz$  section of the apparatus.

## II. EXPERIMENTAL PLATFORM

The experimental platform consists of a bosonic gas of  $^{23}\text{Na}$  atoms, trapped in the elongated optical trap potential generated by a single far-detuned infrared (1064 nm) laser beam, and therefore equal for all spin components. A thermal sample is loaded in the optical trap and presents a Gaussian spatial density distribution in all three directions. In the optical trap ( $\omega_x/2\pi \sim 10$  Hz,  $\omega_{y,z}/2\pi \sim 1$  kHz), the cloud has an elongated shape with a 1:100 aspect ratio, having the long axis along  $x$  and the short axes along  $y$  and  $z$ .

The sample is prepared inside a magnetic shield, which guarantees the stability of the magnetic field at the  $\mu\text{G}$  level [35, 38]. Pairs of magnetic coils inside the innermost layer of the magnetic shield allow for the application of controllable magnetic fields in each of the three spatial directions. Figure 1 schematically represents the apparatus and shows the glass cell, coils, and magnetic shield. The applied magnetic field's stability is ensured using high-stability current supplies [Stanford research system (SRS) LDC501 for the longitudinal field and Delta Elektronika ES 015-10 with 10:1 current dividers for transverse fields]. Ramping from positive to negative values of the longitudinal field within the same experimental run is achieved using two unipolar current supplies with opposite orientations arranged in parallel. A master SRS is set to the steady drive of 100 mA ( $\sim 245$  mG), while a second SRS introduces a tunable current in the opposite direction.

## III. MEASUREMENT SCHEME

Spectroscopic methods are typical solutions to measure a magnetic field. They consist of interrogating an atomic two-level system with constant radiation at different frequencies for a given time and recording the resulting energy spectrum. In such measurements, the

Fourier broadening does not represent a limitation at high magnetic fields when the Zeeman splitting ( $\sim 700$  kHz/G for atomic  $^{23}\text{Na}$ ) is much larger than the resonance linewidth. Conversely, when approaching the  $\mu\text{G}$  regime, resolving the Zeeman structure and exerting suitable control on the polarization of the coupling field becomes challenging.

An alternative method to characterize the magnetic field around the null value relies on ramps of the magnetic field amplitude and directions, taking advantage of the adiabatic/diabatic dynamics of the atomic spin rotation. At low magnetic field, *i.e.*, when the Larmor frequency is of the order or lower than the velocity of rotation of the magnetic field direction, LZ theory [39, 40] applies, resulting in a powerful tool for the magnetic field characterization.

We developed two protocols based on LZ sweeps on the  $z$  (taken as a quantization axis) component of the field. The first one aims to minimize the magnetic field in the transverse  $xy$  plane and is implemented by ramping (or sweeping) the  $z$  field component from positive to negative finite values. The second protocol involves a ramp with a variable endpoint to find the minimum field along  $z$ .

In the following, we will use the magnetic field nomenclature presented in Tab. I.

$B$	Magnetic field modulus
$B_i$ ( $i = x, y, z$ )	Actual magnetic field components
$B_{\perp}$	Transverse field
$B_z$	Longitudinal field
$B_{i,\text{coils}}$	Field induced by the $i$ coil
$B_{i,\text{ramp}}$	Starting $B_{i,\text{coils}}$ of the LZ ramps
$B_{i,0}$	Optimal $B_{i,\text{coils}}$ from fit
$B_{z,c}$	Field set during condensation
$B_{z,\text{fin}}$	Final value of longitudinal field protocol

TABLE I. Magnetic field nomenclature

### A. Energy levels and Landau-Zener theory

The hyperfine ground state of sodium has a total angular momentum  $F = 1$  with three magnetic sublevels  $m_F = 0, \pm 1$  defined as the projection of  $F$  along the  $z$ -axis. The energy of the three states can be estimated with high accuracy using the Breit-Rabi formula [41] once the magnetic field value is known, and, in the small field limit, a linear dependence on the field (first order Zeeman regime) is expected. Let us consider  $z$  as the quantization axis and the magnetic field with a finite transverse component  $B_{\perp} = (B_x^2 + B_y^2)^{1/2}$ . If  $B_z$  is linearly ramped with a slope  $\dot{B}_z$ , from large positive to large negative values passing across zero, the energy of the states as a function of time is the one shown in Fig. 2. At  $B_z = 0$ , the magnetic field is equal to  $B_{\perp}$ , which introduces an avoided crossing between the states.

The time-dependent Hamiltonian of the system for the

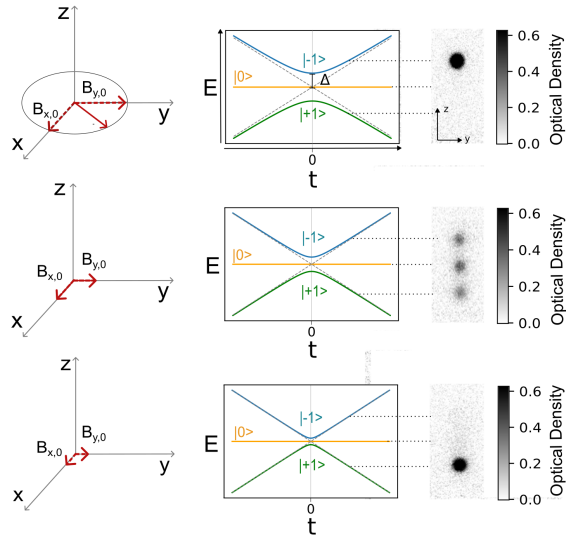


FIG. 2. Transverse field and LZ ramps. For each row, the left panels show a schematic view of the transverse magnetic field components ( $B_{\perp}$  decreases from top to bottom). Central panels show the energy of the three states  $m_F = 0, \pm 1$  as a function of time for the corresponding  $B_{\perp}$ . The right panels show the relative populations of the atoms in the three states at the end of the ramp, obtained experimentally and measured through Stern-Gerlach imaging. For the three different values of  $B_{\perp}$  we obtain full adiabatic transfer (upper panel, large  $B_{\perp}$ ), partial transfer (central panel), and complete diabatic transfer (lower panel, low  $B_{\perp}$ ).

wavefunction  $\{\psi_{-1}, \psi_0, \psi_{+1}\}$  reads

$$H(t) = g_F \mu_B \begin{pmatrix} \alpha t & \Delta & 0 \\ \Delta & 0 & \Delta \\ 0 & \Delta & -\alpha t \end{pmatrix}, \quad (1)$$

where  $g_F = -1/2$  is the Landé factor,  $\mu_B$  is the Bohr magneton, and  $\Delta = B_{\perp}/\sqrt{2}$  acts as a coupling between the states and defines the gap in the energy levels shown in Fig. 1. Here  $t = 0$  is defined as the instant when  $B_z = 0$ . The parameter  $\alpha$  originates from the time derivative of the Larmor frequency at the energy levels crossing

$$\alpha = \left| |B(t)| \frac{\partial}{\partial t} \left( \arctan \frac{\dot{B}_z t}{|B(t)|} \right) \right|_{t=0} = |\dot{B}_z|. \quad (2)$$

While the atoms are initially prepared in the  $m_F = -1$  at large (as compared to  $B_{\perp}$ ), positive values of  $B_z$ , ramping  $B_z$  in time may induce the transfer to different  $m_F$  states according to the analytical model discussed in [34]. In the following, we apply the results of [42] as we measure the  $m_F$  population distribution at long times after the inversion of  $B_z$ :

$$P_1 = p^2, \quad (3)$$

$$P_0 = 2p(1-p), \quad (4)$$

$$P_{-1} = (1-p)^2, \quad (5)$$

with

$$p = e^{-2\pi |g_F| \mu_B \frac{\Delta^2}{\hbar \alpha}} \quad (6)$$

being the LZ transfer probability. From Eq. (3) and Eq. (6), one finds that a complete diabatic transfer of the population from the  $m_F = -1$  to the  $m_F = +1$  state takes place when  $p \approx 1$  (large ramp speed  $\alpha$  or small gap  $\Delta$ ), while adiabaticity is preserved for small  $\alpha$  and large  $\Delta$ . This results from implementing the adiabatic condition to the spin dynamics in a rotating magnetic field. In other words, adiabaticity is fulfilled when the variation of the magnetic field direction is smaller than the Larmor frequency, *i.e.*,  $|\dot{B}_z/B| \ll |g_F \mu_B B/\hbar|$ . For instance, the probability of the transition to  $m_F = 1$  has a Gaussian distribution with RMS width  $\frac{\sigma_B}{\sqrt{2}}$  where  $\sigma_B = (\dot{B}_z \hbar / (2\pi |g_F| \mu_B))^{1/2}$  is defined from the LZ transfer probability and it is the width used in the following.

## B. Experimental protocols

### 1. Transverse field minimization

The goal is to find the optimal current values for each coil to compensate for the residual transverse magnetic

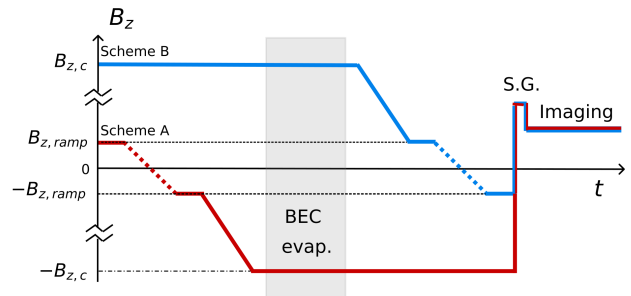


FIG. 3. Transverse field minimization protocol.  $B_z$  is shown as a function of time. Scheme A (red line) consists in a ramp from  $B_{z,\text{ramp}}$  to  $-B_{z,\text{ramp}}$  performed on a thermal cloud, then  $B_z$  is brought down to  $-B_{z,c}$  in 50 ms before the evaporation in the optical trap. Scheme B (blue line) starts with the condensation at a finite value of the field  $B_{z,c}$ , then after the evaporation, the field is ramped down to  $B_{z,\text{ramp}}$  in 50 ms. Here the condensate experiences the field ramp across zero, from  $B_{z,\text{ramp}}$  to  $-B_{z,\text{ramp}}$ . In both cases, the dotted line corresponds to the field crossing the minimum value with a tunable ramp duration. The shaded gray area denotes the time during which the sample is evaporated to obtain a BEC.

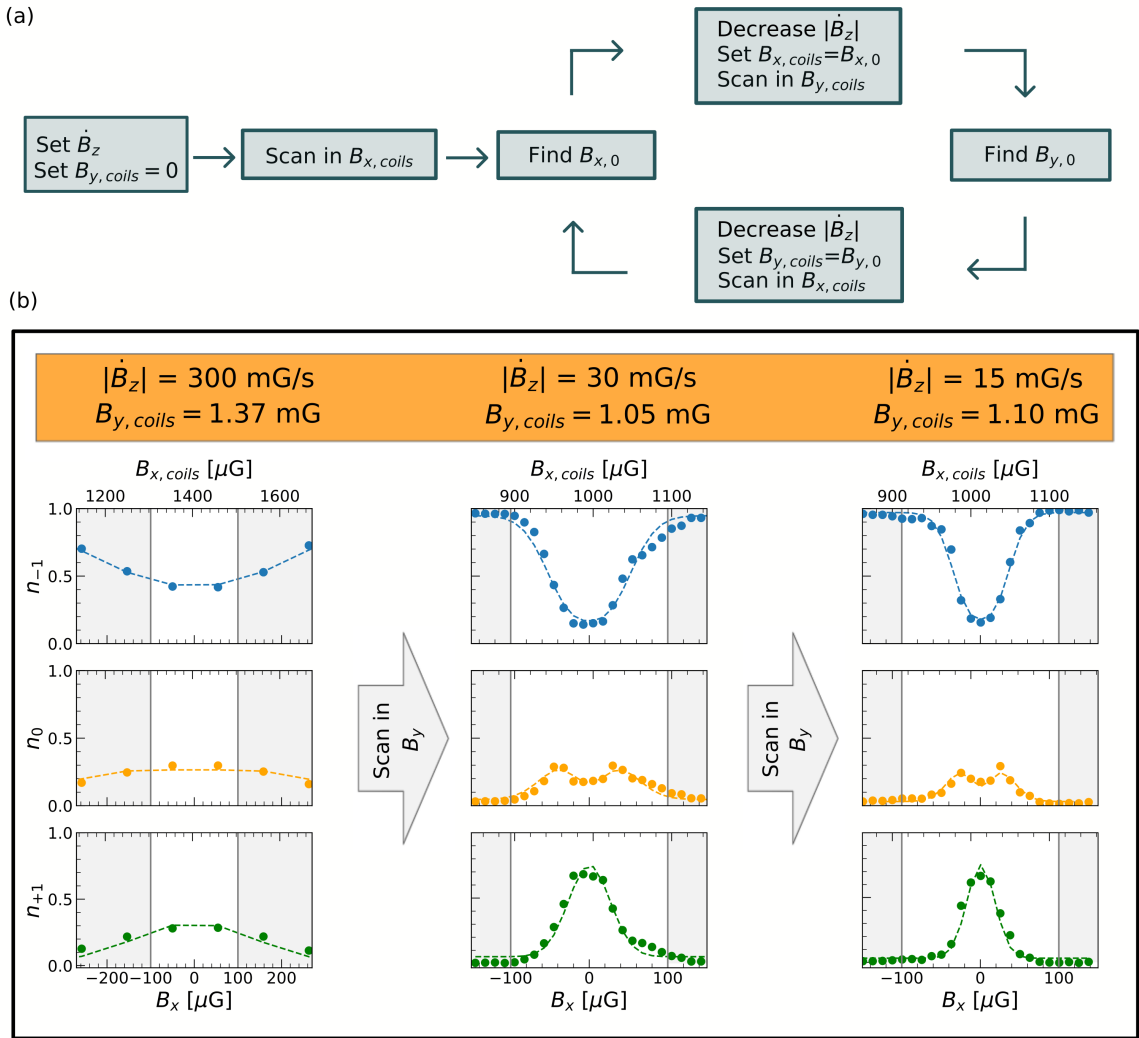


FIG. 4. Transverse field determination. (a) Schematic representation of the iterative measurement process; see main text. (b) Relative populations of the three Zeeman levels  $m_F = -1, 0, +1$  (from top to bottom) for decreasing ramp velocities  $\alpha$  (from left to right). All panels show the experimental data (dots) and the fitted function (solid line) plotted as a function of the transverse field in the  $x$  directions. For each panel, the upper axis shows the field's value generated by the coils, while the lower axis is shifted according to the fit result. The speed of the ramp is specified in the orange box as well as the value of the compensating field in the  $y$  direction used for each scan. Note the offset of the compensating field in the first column, whose data were acquired with a few weeks delay with respect to the other two data sets.

field (which is not screened by the magnetic shield or due to the shield's permanent magnetization).

The protocol to minimize the transverse field amplitude  $B_{\perp}$  starts with a thermal atomic sample by setting the values of the currents in the coils for the transverse directions, generating the fields  $B_{x,coils}$  and  $B_{y,coils}$ . In the following, we discuss the two experimental schemes depicted in Fig. 3.

Scheme A (red line) consists in changing  $B_z$  from  $B_{z,ramp}$  to  $-B_{z,ramp}$  with a linear ramp of variable duration  $\Delta t^*$ . After this first ramp,  $B_z$  is reduced to  $-B_{z,c} \approx -130$  mG  $\ll -B_{z,ramp}$  in 50 ms. Then, the sample is evaporatively cooled to Bose condensation by re-

ducing the dipole trapping beam intensity. To image the spin state, after switching off the trapping potential, a vertical magnetic field gradient of 8 G/cm is applied to separate the three states in a Stern-Gerlach-like scheme. A simultaneous absorption image of the three states is made after a time-of-flight of 18 ms. Bose condensing the sample before imaging favors the spatial spin resolution of the Stern-Gerlach imaging, given the relatively small amount of the applied magnetic field gradient and ballistic expansion time.

To reduce the sensitivity to magnetic field inhomogeneities, in Scheme B (blue line) the order between LZ ramp and evaporation is reversed. The atomic sample is

first cooled below the critical temperature for condensation at  $B_{z,c} \approx 130$  mG, and then the field is decreased to  $B_{z,\text{ramp}}$  to apply the LZ ramp from  $B_{z,\text{ramp}}$  to  $-B_{z,\text{ramp}}$ . By doing so, the spatial extent of the condensed atomic sample is considerably smaller during the LZ ramp, suppressing the contributions from the magnetic field's spatial inhomogeneities.

The ramp duration  $\Delta t^*$  should be much longer than the coils time constant  $\tau = L/R \simeq 0.5$  ms, where  $L$  and  $R$  are the inductance and the resistance of the coils, respectively, and much shorter than the sample lifetime in the trap ( $\tau_{\text{BEC}} \simeq 1$  s,  $\tau_{\text{th}} \gg 1$  s). The value  $B_{z,\text{ramp}}$  was chosen depending on the ramp duration, from a maximum of 1.5 mG to a minimum of  $750 \mu\text{G}$ , with  $|\dot{B}_z|$  ranging from a maximum of 3 G/s to a minimum of 3.75 mG/s.

The values  $B_{x,0}$  and  $B_{y,0}$  that best compensate for the residual transverse field are the ones giving the maximal transfer to the  $m_F = +1$  state. They are found through an iterative procedure, as sketched in Fig. 4a. The first iteration is a scan in  $B_{x,\text{coils}}$  setting  $|\dot{B}_z| = 300$  mG/s and  $B_{y,\text{coils}} = 0$ . We obtain the value  $B_{x,0}$  for which we observe maximum transfer in  $m_F = +1$ . Then, we set  $B_{x,\text{coils}} = B_{x,0}$  and we perform a scan in  $B_{y,\text{coils}}$  obtaining  $B_{y,0}$  for which we have the maximal transfer of the population in the state  $m_F = +1$ . We repeat this procedure by slowing down the ramp in  $B_z$  at each iteration. In this way, the  $P_{+1}$  distribution shrinks, increasing our sensitivity to determine the field value that best compensates for the residual one. The first iteration starts finding the value  $B_{x,0}$  with a scan in  $B_{x,\text{coils}}$  at fixed  $B_{y,\text{coils}} = 0$ , with a given ramp speed  $|\dot{B}_z| = 300$  mG/s. Then, at fixed  $B_{x,\text{coils}} = B_{x,0}$  we perform a scan in  $B_{y,\text{coils}}$  obtaining  $B_{y,0}$ .

Figure 4b presents the three hyperfine relative populations,  $n_{-1}$ ,  $n_0$ ,  $n_{+1}$ , for three subsequent scans of the magnetic field  $B_{x,\text{coils}}$ , with decreasing value of  $|\dot{B}_z|$  and  $B_{y,\text{coils}}$  set to the value determined in the previous iteration step. The experimental data were fitted to Eq. (3-5) from which we extract the center  $B_{x,0}$ , the maximum transfer  $P_{1,\text{max}}$ , and the width  $\sigma_B$  of the transfer peak. At first, the center of the observed structures corresponds to  $B_x = 0$  and this allows us to determine  $B_{x,\text{coils}}$  to compensate any residual field along  $x$ . The maximum in the transferred population  $P_{1,\text{max}}$  depends on the residual field in  $y$ ,

$$B_y = \sqrt{-\frac{\hbar \dot{B}_z}{\pi \mu_B} \ln(P_{1,\text{max}})}, \quad (7)$$

which is minimized after each  $B_x$  scan (scan in  $B_{y,\text{coils}}$  are not shown in figure). As expected, slower ramps lead to smaller  $\sigma_B$  (as highlighted by the white windows, which always mark a region of  $200 \mu\text{G}$ ), and consequently to increase the precision at which  $B_x = 0$  (and  $B_y$ ) is determined.

## 2. Longitudinal field

The protocol presented in the previous section allows for minimizing the transverse magnetic field. The best-obtained values are then used as transverse fields setting  $B_{x,\text{coils}} = B_{x,0}$  and  $B_{y,\text{coils}} = B_{y,0}$  for the characterization of the residual longitudinal field  $B_z$ .

Here, we introduce the procedure to characterize the residual longitudinal field  $B_z$ . The gas is first evaporated to obtain a BEC at  $B_{z,c} = 130$  mG, then  $B_{z,\text{coils}}$  is ramped from a positive value  $B_{z,\text{ramp}}$  down to a variable one  $B_{z,\text{fin}}$  with constant ramp  $\dot{B}_z = -15$  mG/s. As the Stern-Gerlach imaging is implemented at positive  $B_z$ , we constrain the diabatic spin dynamics to the decreasing ramp on  $B_{z,\text{coils}}$  by raising the transverse field to a finite value after the end of the  $B_{z,\text{coils}}$  ramp, see Fig. 5. If  $B_{z,\text{fin}} > 0$ , the LZ transfer does not take place since the ramp is interrupted before the zero crossing on  $B_{z,\text{coils}}$  hence leaving the atoms in  $m_F = -1$ . If  $B_{z,\text{coils}} < 0$ , on the other hand, the transfer to  $m_F = +1$  takes place. An example of such a scan is given in Fig. 6 where the relative populations in the three states are represented as a function of the value  $B_{z,\text{fin}}$ . We verified that using a slower ramp does not affect the experimental result.

## IV. RESULTS

From the fits of the experimental data, as the examples shown in Fig. 4, it is possible to extract both the width of the transfer peak  $\sigma_B$  and, from the contrast of the LZ population transfer, the residual transverse magnetic

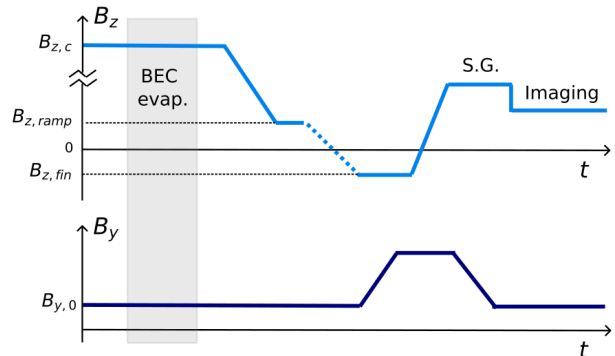


FIG. 5. Longitudinal field protocol. Representation of the field in  $z$  and  $y$  directions. For the field in the longitudinal direction, the protocol is analogous to Scheme B with the only difference that the speed of the ramp is fixed to be  $\dot{B}_z = 15$  mG/s while the final value of the ramp  $B_{z,\text{fin}}$  is varied. The field in the  $y$ -direction is fixed to the optimal value  $B_{y,0}$  previously determined, it is adiabatically ramped to a finite value and then back to  $B_{y,0}$  for the imaging procedure. The field along  $x$  is not shown in the figure, as it is kept at a constant value  $B_{x,0}$  for the whole duration of the experiment.

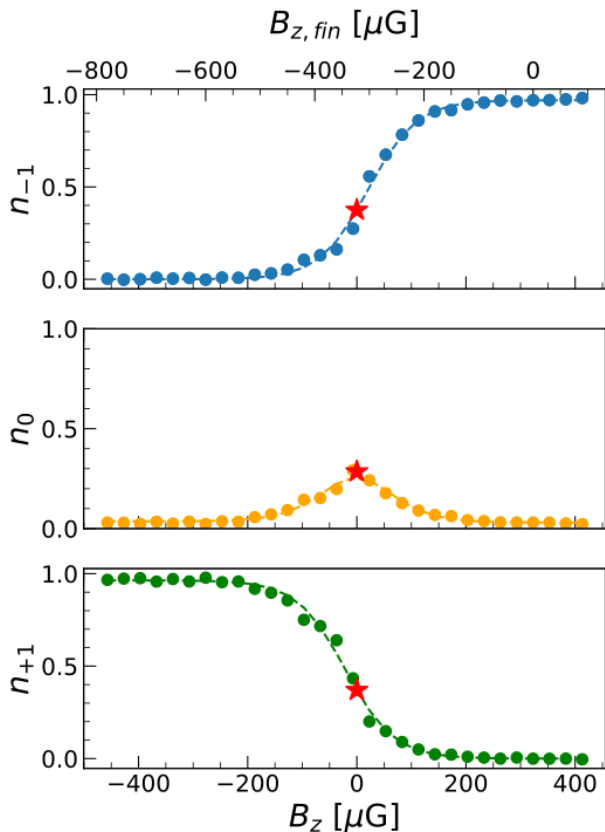


FIG. 6. Example of the longitudinal field characterization. Each panel shows the relative population for the three states as a function of  $B_{z,\text{fin}}$ . The dots are experimental data obtained averaging different experimental realizations, with standard deviation smaller than the marker size, while dotted line is the result of the sigmoidal fit. The value  $B_{z,0}$  compensating for the residual field is pointed by the red star.

field  $B_{\perp}$ . Figure 7a shows the measured width  $\sigma_B$  of the transfer peak as a function of  $|\dot{B}_z|$  for both protocols (red symbols for A and blue for B). Each point was obtained by averaging the widths from different experimental runs with the same ramp speed. The experimental values of the width are consistent with  $\sigma_B$  predicted from the LZ theory (dashed line in the figure). We attribute the general increase in the experimental values to effects not included in the LZ discussed so far.

For instance, comparing the measurements taken on a thermal sample (empty red symbols in Fig. 7) to the ones taken on the smaller Bose condensed sample (empty blue symbols), the flattening trend of  $\sigma_B$  observed with the thermal sample around  $30 \mu\text{G}$  can be attributed to magnetic field inhomogeneities, *i.e.* magnetic field gradients along the elongated direction of the atomic sample  $y$ . Here, the residual magnetic field difference between opposite regions gives rise to an additional contribution  $\sigma_{\text{grad}}$  in the determination of  $\sigma_B$ , which we expect to sum

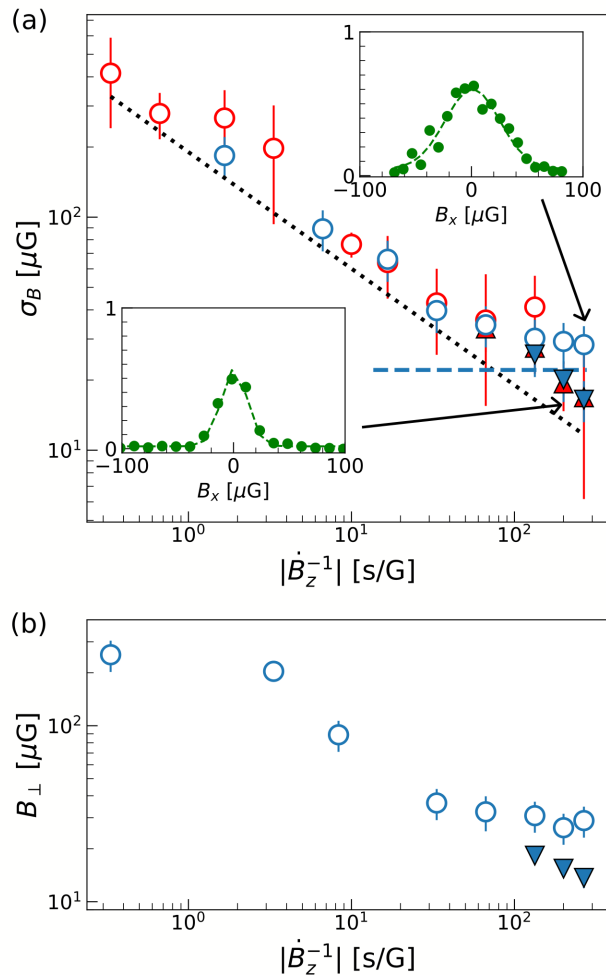


FIG. 7. a) Width  $\sigma_B$  of LZ transfer probability as a function of the ramp speed. The dashed black line is the theoretical prediction from LZ theory; the symbols are the experimental results using scheme A (red symbols) or scheme B (blue symbols). Empty (filled) symbols are obtained without (with) compensation for the residual gradient, respectively. The error bars have been estimated considering the fluctuations of different datasets. The two insets are examples of the population in the state  $m_F = +1$  obtained at a ramp velocity of  $3.75 \text{ mG/s}$  with (left inset) and without (right inset) the compensation of the gradient. The blue dashed line is the contribution of the residual magnetic field gradient to the peak width. b) Transverse residual magnetic field  $B_{\perp}$  extracted from the population fits as a function of the inverse of the ramp velocities. Note that the error bars for the data obtained compensating the magnetic field inhomogeneities are too small to be seen in the plot.

in quadrature with  $\sigma_{\text{LZ}}$  predicted by the LZ theory:

$$\sigma_B = \sqrt{\sigma_{\text{LZ}}^2 + \sigma_{\text{grad}}^2}. \quad (8)$$

We determine the optimal compensation for this gradient by employing a dedicated set of coils in anti-Helmholtz configuration, which is driven to reduce  $\sigma_B$

further (inset in Fig. 7a, and filled dots in 7a and b). From Eq. (8) and the comparison between data with and without compensation obtained with protocol B, we estimate the non-compensated gradient contribution at  $\sigma_{\text{grad}} = 22 \pm 3 \mu\text{G}$  (horizontal dashed blue line in Fig. 7a). This is consistent with the estimation from cloud size and magnetic field gradient applied to minimize  $\sigma_B$ . We notice that  $\sigma_B$  acquired in schemes A and B are comparable upon magnetic gradient compensation.

In Fig. 7b, we plot  $B_{\perp}$  obtained by fitting Eq. (7) on the experimental data both for measurements without (empty symbols) and with (filled triangles) the gradient compensation. The smallest width observed allows us to determine the minimal residual transverse field at  $14 \pm 2 \mu\text{G}$ , a value that could be limited by the noise of the current supplies driving the compensation coils. Also, it is worth mentioning that the condition for the residual field compensation has generally been stable for several weeks. Still, we did observe jumps in the compensation field at the level of hundreds of  $\mu\text{G}$  (a few events over six months of measurements), which we could not clearly attribute to technical circumstances.

The longitudinal field was minimized by following the protocol explained in Sec. III B 2.  $B_{z,0}$  is chosen as the center of the sigmoidal fit of the data shown in Fig. 6,  $B_{z,0} = -323 \pm 10 \mu\text{G}$ .

By combining the minimal transverse and longitudinal field results, we estimate we can reach a minimal field modulus of  $18 \pm 5 \mu\text{G}$ , which complies with the conditions for observing a nematic phase in a  $^{23}\text{Na}$  BEC.

## V. CONCLUSIONS AND OUTLOOK

In this paper, we present a technique to characterize and compensate magnetic fields at the level of  $10 \mu\text{G}$  in experiments with ultracold atomic gases. The method is based on monitoring the Zeeman populations in diabatic atomic spin rotation. The simulations based on the LZ dynamics for a three-level system reproduced the experimental data well. These results pave the way to studying the unexplored scenario of condensation in zero magnetic fields in extended spinor gases, when spin interactions may become dominant over all other contributions of the Hamiltonian. For instance, the ground state of F=1 BEC characterized by antiferromagnetic interaction is expected to develop an order parameter with a nematic character, which has not been reported on superfluid matter so far.

## ACKNOWLEDGEMENTS

We acknowledge funding from Provincia Autonoma di Trento, from the European Union's Horizon 2020 research and innovation Programme through the STAQS project of QuantERA II (Grant Agreements No. 101017733 and No. 101017733) and from the European Union - Next Generation EU through PNRR MUR project PE0000023-NQSTI. This work was supported by Q@TN, the joint lab between the University of Trento, FBK - Fondazione Bruno Kessler, INFN - National Institute for Nuclear Physics and CNR - National Research Council.

- 
- [1] T. Mulvey, Origins and historical development of the electron microscope, *British Journal of Applied Physics* **13**, 197 (1962).
  - [2] E. Ruska, The development of the electron microscope and of electron microscopy, *Rev. Mod. Phys.* **59**, 627 (1987).
  - [3] O. Krivanek, G. Corbin, N. Dellby, B. Elston, R. Keyse, M. F. Murfitt, C. Own, Z. Szilagy, and J. Woodruff, An electron microscope for the aberration-corrected era, *Ultramicroscopy* **108**, 179 (2008).
  - [4] E. Rasel, W. Schleich, and S. Wölk, eds., *Atom interferometry and its applications* (IOS, Amsterdam; SIF, Bologna 2019) pp. 345–392, Proceedings of the International School of Physics “Enrico Fermi”, Course CXC VII, Varenna, 8-13 July 2016.
  - [5] P. Mansfield and B. Chapman, Multishield active magnetic screening of coil structures in NMR, *Journal of Magnetic Resonance* **72**, 211 (1987).
  - [6] A. D. Ludlow, M. M. Boyd, J. Ye, E. Peik, and P. O. Schmidt, Optical atomic clocks, *Rev. Mod. Phys.* **87**, 637 (2015).
  - [7] E. Nicklas, M. Karl, M. Höfer, A. Johnson, W. Muesel, H. Strobel, J. Tomkovič, T. Gasenzer, and M. K. Oberthaler, Observation of scaling in the dynamics of a strongly quenched quantum gas, *Phys. Rev. Lett.* **115**, 245301 (2015).
  - [8] A. Farolfi, A. Zenesini, R. Cominotti, D. Trypogeorgos, A. Recati, G. Lamporesi, and G. Ferrari, Manipulation of an elongated internal Josephson junction of bosonic atoms, *Phys. Rev. A* **104**, 023326 (2021).
  - [9] A. Farolfi, A. Zenesini, D. Trypogeorgos, C. Mordini, A. Gallemí, A. Roy, A. Recati, G. Lamporesi, and G. Ferrari, Quantum-torque-induced breaking of magnetic interfaces in ultracold gases, *Nat. Phys.* **17**, 1359 (2021).
  - [10] M. P. Ledbetter, I. M. Savukov, D. Budker, V. Shah, S. Knappe, J. Kitching, D. J. Michalak, S. Xu, and A. Pines, Zero-field remote detection of nmr with a microfabricated atomic magnetometer, *Proceedings of the National Academy of Sciences* **105**, 2286 (2008).
  - [11] M. Tayler, T. Theis, T. Sjolander, J. Blanchard, A. Kentner, S. Pustelny, A. Pines, and D. Budker, Instrumentation for nuclear magnetic resonance in zero and ultralow magnetic field, Review of Scientific Instruments **88**, 10.1063/1.5003347 (2017).
  - [12] G. L. Romani, S. J. Williamson, and L. Kaufman, Bio-magnetic instrumentation, *Review of Scientific Instru-*

- ments **53**, 1815 (1982).
- [13] J. Dupont-Roc, S. Haroche, and C. Cohen-Tannoudji, Detection of very weak magnetic fields ( $10^{-9}$  G) by  $^{87}\text{Rb}$  zero-field level crossing resonances, *Physics Letters A* **28**, 638 (1969).
- [14] D. Budker, W. Gawlik, D. F. Kimball, S. M. Rochester, V. V. Yashchuk, and A. Weis, Resonant nonlinear magneto-optical effects in atoms, *Rev. Mod. Phys.* **74**, 1153 (2002).
- [15] D. Budker and M. Romalis, Optical magnetometry, *Nature Physics* **3**, 227 (2007).
- [16] A. Meraki, L. Elson, N. Ho, A. Akbar, M. Koźbial, J. Kołodyński, and K. Jensen, Zero-field optical magnetometer based on spin alignment, *Phys. Rev. A* **108**, 062610 (2023).
- [17] M. Brookes, J. Leggett, M. Rea, R. Hill, N. Holmes, E. Boto, and R. Bowtell, Magnetoencephalography with optically pumped magnetometers (OPM-MEG): the next generation of functional neuroimaging, *Trends Neuroscience* **8**, 621 (2022).
- [18] T. Sander, J. Preusser, R. Mhaskar, J. Kitching, L. Trahms, and S. Knappe, Magnetoencephalography with a chip-scale atomic magnetometer, *Biomed Opt Express* **3**, 981 (2012).
- [19] P. Bevington, R. Gartman, and W. Chalupczak, Enhanced material defect imaging with a radio-frequency atomic magnetometer, *Journal of Applied Physics* **125**, 094503 (2019).
- [20] L. Rushton, T. Pyragius, A. Meraki, L. Elson, and K. Jensen, Unshielded portable optically pumped magnetometer for the remote detection of conductive objects using eddy current measurements, *Review of Scientific Instruments* **93**, 125103 (2022).
- [21] M. V. Romalis and H. B. Dang, Atomic magnetometers for materials characterization, *Materials Today* **14**, 258 (2011).
- [22] M. W. Mitchell and S. Palacios Alvarez, Colloquium: Quantum limits to the energy resolution of magnetic field sensors, *Rev. Mod. Phys.* **92**, 021001 (2020).
- [23] T. Isayama, Y. Takahashi, N. Tanaka, K. Toyoda, K. Ishikawa, and T. Yabuzaki, Observation of larmor spin precession of laser-cooled rb atoms via paramagnetic faraday rotation, *Phys. Rev. A* **59**, 4836 (1999).
- [24] Y. Cohen, K. Jadeja, S. Sula, M. Venturelli, C. Deans, L. Marmugi, and F. Renzoni, A cold atom radio-frequency magnetometer, *Applied Physics Letters* **114**, 073505 (2019).
- [25] J. M. Higbie, L. E. Sadler, S. Inouye, A. P. Chikkatur, S. R. Leslie, K. L. Moore, V. Savalli, and D. M. Stamper-Kurn, Direct nondestructive imaging of magnetization in a spin-1 bose-einstein gas, *Phys. Rev. Lett.* **95**, 050401 (2005).
- [26] S. Wildermuth, S. Hofferberth, I. Lesanovsky, S. Groth, P. Krüger, J. Schmiedmayer, and I. Bar-Joseph, Sensing electric and magnetic fields with Bose-Einstein condensates, *Applied Physics Letters* **88**, 264103 (2006).
- [27] M. Vengalattore, J. M. Higbie, S. R. Leslie, J. Guzman, L. E. Sadler, and D. M. Stamper-Kurn, High-resolution magnetometry with a spinor bose-einstein condensate, *Phys. Rev. Lett.* **98**, 200801 (2007).
- [28] O. Eliasson, R. Heck, J. S. Laustsen, M. Napolitano, R. Müller, M. G. Bason, J. J. Arlt, and J. F. Sherson, Spatially-selective in situ magnetometry of ultracold atomic clouds, *Journal of Physics B: Atomic, Molecular and Optical Physics* **52**, 075003 (2019).
- [29] D. M. Stamper-Kurn and M. Ueda, Spinor Bose gases: Symmetries, magnetism, and quantum dynamics, *Rev. Mod. Phys.* **85**, 1191 (2013).
- [30] K. Jiménez-García, A. Invernizzi, B. Evrard, C. Frapolli, J. Dalibard, and F. Gerbier, Spontaneous formation and relaxation of spin domains in antiferromagnetic spin-1 condensates, *Nature Communication* **10**, 1422 (2019).
- [31] B. Pasquiou, E. Maréchal, G. Bismut, P. Pedri, L. Vernac, O. Gorceix, and B. Laburthe-Tolra, Spontaneous Demagnetization of a Dipolar Spinor Bose Gas in an Ultralow Magnetic Field, *Phys. Rev. Lett.* **106**, 255303 (2011).
- [32] M. Fattori, G. Roati, B. Deissler, C. D'Errico, M. Zaccanti, M. Jona-Lasinio, L. Santos, M. Inguscio, and G. Modugno, Magnetic dipolar interaction in a bose-einstein condensate atomic interferometer, *Phys. Rev. Lett.* **101**, 190405 (2008).
- [33] B. Evrard, A. Qu, J. Dalibard, and F. Gerbier, Observation of fragmentation of a spinor bose-einstein condensate, *Science* **373**, 1340 (2021).
- [34] Y. B. Band and Y. Avishai, Three-level Landau-Zener dynamics, *Phys. Rev. A* **99**, 032112 (2019).
- [35] A. Farolfi, D. Trypogeorgos, G. Colzi, E. Fava, G. Lamporesi, and G. Ferrari, Design and characterization of a compact magnetic shield for ultracold atomic gas experiments, *Review of Scientific Instruments* **90**, 115114 (2019).
- [36] R. Cominotti, A. Berti, C. Dulin, C. Rogora, G. Lamporesi, I. Carusotto, A. Recati, A. Zenesini, and G. Ferrari, Ferromagnetism in an Extended Coherently Coupled Atomic Superfluid, *Phys. Rev. X* **13**, 021037 (2023).
- [37] A. Zenesini, A. Berti, R. Cominotti, C. Rogora, I. G. Moss, T. P. Billam, I. Carusotto, G. Lamporesi, A. Recati, and G. Ferrari, False vacuum decay via bubble formation in ferromagnetic superfluids, *Nature Physics* **20**, 558 (2024).
- [38] G. Colzi, E. Fava, M. Barbiero, C. Mordini, G. Lamporesi, and G. Ferrari, Production of large Bose-Einstein condensates in a magnetic-shield-compatible hybrid trap, *Phys. Rev. A* **97**, 053625 (2018).
- [39] L. Landau, Zur theorie der energieubertragung ii, *Zeitschrift fur Physik (Sowjetunion)* **2**, 46 (1932).
- [40] C. Zener, Non-adiabatic crossing of energy levels, *Proc. R. Soc. Lond.* **A137**, 696–702 (1932).
- [41] G. Breit and I. I. Rabi, Measurement of nuclear spin, *Phys. Rev.* **38**, 2082 (1931).
- [42] C. E. Carroll and F. T. Hioe, Transition probabilities for the three-level landau-zener model, *Journal of Physics A: Mathematical and General* **19**, 2061 (1986).